

See discussions, stats, and author profiles for this publication at: <https://www.researchgate.net/publication/231667515>

Surface-Enhanced Raman Scattering on Hierarchical Porous Cuprous Oxide Nanostructures in Nanoshell and Thin-Film Geometries

ARTICLE in JOURNAL OF PHYSICAL CHEMISTRY LETTERS · FEBRUARY 2012

Impact Factor: 7.46 · DOI: 10.1021/jz201694s

CITATIONS

31

READS

62

4 AUTHORS, INCLUDING:



Chao Qiu

University of New Mexico

8 PUBLICATIONS 128 CITATIONS

SEE PROFILE



Hui Wang

University of South Carolina

34 PUBLICATIONS 385 CITATIONS

SEE PROFILE



Chaoyang Jiang

University of South Dakota

66 PUBLICATIONS 2,859 CITATIONS

SEE PROFILE

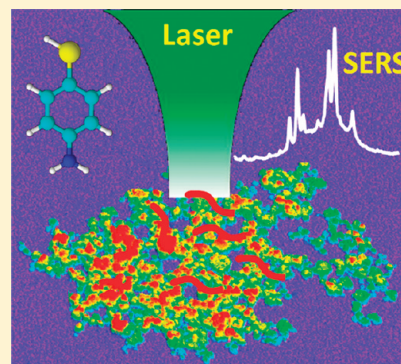
Surface-Enhanced Raman Scattering on Hierarchical Porous Cuprous Oxide Nanostructures in Nanoshell and Thin-Film Geometries

Chao Qiu,[†] Li Zhang,[‡] Hui Wang,^{*,‡} and Chaoyang Jiang^{*,†}[†]Department of Chemistry, University of South Dakota, Vermillion, South Dakota 57069, United States[‡]Department of Chemistry and Biochemistry, University of South Carolina, Columbia, South Carolina 29208, United States

S Supporting Information

ABSTRACT: Understanding the mechanism of surface-enhanced Raman scattering (SERS) of molecules on semiconductor nanostructures is directly related to our capabilities of designing and optimizing new SERS-active substrates for broad applications in the field of molecular detection and characterization. Here, we present an exploration of using cuprous oxide nanostructures with hierarchical porosity for enhancing Raman signals of adsorbed probe molecules. Distinct SERS signals were detected on both individual polycrystalline nanoshells and porous thin films composed of cuprous oxide nanocrystals. The observed enhancement of SERS signals can be interpreted as synergistic effects of strong chemical interactions between the probe molecules and cuprous oxide surfaces, localized electromagnetic field enhancement, and the unique hierarchical porosity of the nanostructures. Our work introduced a novel type of semiconductor substrates for high-performance SERS and extended the applications of cuprous oxide nanostructures to spectroscopy-based molecular sensing and characterizations.

SECTION: Nanoparticles and Nanostructures



Since its discovery in the mid 1970s,^{1–3} surface-enhanced Raman scattering (SERS) has received significant interest, ranging from widespread applications in chemical and biomolecular sensing and fabrication of SERS-active nanostructures to theoretical simulations and aided design of high-performance SERS substrates.^{4–6} Its high detection sensitivity and unique capability of identifying molecular structures make SERS a powerful analytical tool in a broad range of applications. The past two decades have witnessed significant advances in developing new strategies to construct nanostructured substrates with excellent SERS activity and reproducibility.^{7–10} While coinage metals and their alloys, either in the form of roughened surfaces or nanoparticle aggregates, have been extensively used for SERS, recent research in this field is more focused on fine-controlled hierarchical nanostructures that exhibit superior SERS performance.^{11–13} In addition to nanostructures of coinage metals, SERS-active substrates composed of transition metals¹⁴ or semiconductor materials^{15–18} have also emerged, and their enhancement mechanisms have been studied. The emergence of transition-metal and semiconductor nanostructures as SERS-active materials not only advances our fundamental knowledge of Raman enhancement but also expands and facilitates the choice of SERS-active substrates for much broader applications.

Similar to some other semiconductor materials, cuprous oxide (Cu₂O) also has the potential to be a SERS-active substrate; however, comprehensive investigations have not been conducted thus far, and there is still a significant lack of sufficient data for further exploration and optimization. Cu₂O, a

p-type semiconductor with a bulk band gap of 2.2 eV, is an excellent functional material for low-cost photovoltaics,¹⁹ high-efficiency photocatalysis,^{20,21} and other energy-related applications.^{22,23} Cu₂O nanostructures of various geometries have been synthesized through bottom-up approaches,^{24–29} and their unique structure-dependent optical and catalytic properties have been discussed.^{30–32} For example, it has been recently demonstrated that the light absorption and scattering properties of Cu₂O nanoshells can be fine-tuned across the visible and near-infrared spectral regions by tailoring the inner and outer radii of the nanoshells.³¹ The first example of using Cu₂O as SERS substrates was reported by Kudelski and co-workers,³³ who observed SERS of pyridine on both Cu₂O hydrogel suspensions and Cu₂O-coated copper electrodes. It has been recently observed that the Raman signals of 4-mercaptopyridine can be significantly enhanced when the molecules are adsorbed on the surface of Cu₂O/Ag nanocomposites.³⁴ However, to the best of our knowledge, there is no report on the direct use of Cu₂O nanostructures as active substrates for SERS thus far. The relationship between the optical scattering and the SERS enhancement on Cu₂O nanostructures has never been investigated.

In this Letter, we report an exploration of using Cu₂O nanostructures with hierarchical porosity to enhance the Raman signals of adsorbed probe molecules. The SERS performance of

Received: December 25, 2011

Accepted: February 15, 2012

Published: February 15, 2012

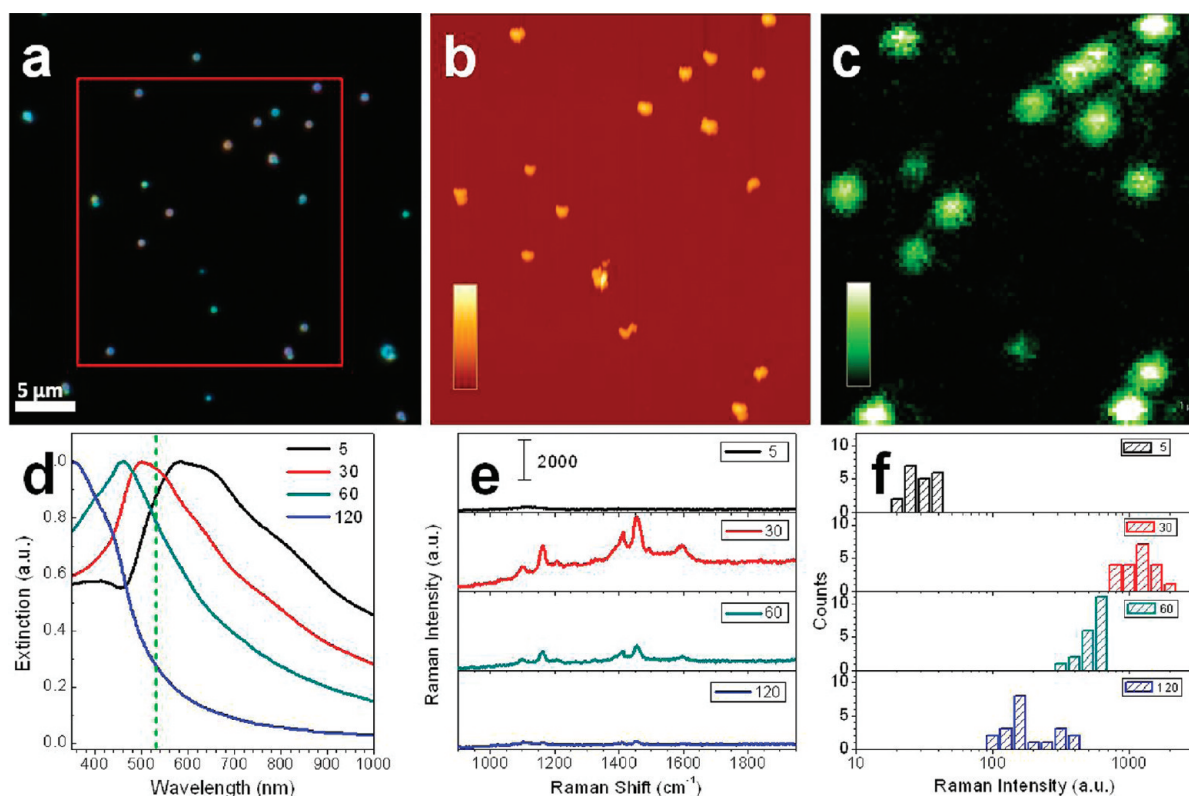


Figure 1. (a) Dark-field optical image of Cu_2O nanoshells (obtained after 30 min of Ostwald ripening) deposited on a glass substrate. The box indicates the area for detailed AFM and confocal Raman study. (b) AFM image; the z scale is 750 nm. (c) Confocal Raman mapping (based on the 1435 cm^{-1} mode); the z scale is 200 counts. (d) Extinction spectra for Cu_2O nanoshells obtained after undergoing Ostwald ripening for 5, 30, 60, and 120 min. The vertical dash line indicates the excitation laser wavelength (532 nm). (e) Representative SERS spectra from individual Cu_2O nanoshells with varying ripening times. (f) Histograms of the Raman intensity (1435 cm^{-1} mode) from individual Cu_2O nanoshells.

both individual polycrystalline nanoshells and planar thin films composed of Cu_2O nanocrystals was evaluated. Strong chemical enhancement for SERS of probe molecules (4-aminothiophenol, 4-ATP) on the surface of the hierarchical Cu_2O nanostructures was observed, together with the enhanced Raman signals from dimercaptoazobenzene (DMAB) molecules, which were formed due to a surface dimerization process. In addition, geometry control of Cu_2O nanoshells through Ostwald ripening allowed us to observe a correlation between the scattering spectra and the SERS enhancements achievable on individual Cu_2O nanoshells. Furthermore, we estimated the electromagnetic contribution to the overall Raman enhancements by performing finite difference time domain (FDTD) simulations on the near-field enhancements of the porous Cu_2O hierarchical nanostructures upon optical excitation.

Geometry-dependent optical properties and SERS performance of individual Cu_2O nanoshells were systematically studied using a combination of dark-field optical microscopy, atomic force microscopy (AFM), and confocal Raman microscopy. Polycrystalline Cu_2O nanoshells were synthesized following the method reported recently,³¹ and their optical properties could be fine-tuned by varying the time of Ostwald ripening. Cu_2O nanoshells obtained after a 30 min Ostwald ripening process were first deposited on a glass substrate and incubated in a 0.8 mM 4-ATP solution for further characterization (see Supporting Information for details). Figure 1a shows the dark-field optical image of Cu_2O nanoshells on glass, where isolated nanoshells can be visualized. The AFM image of the same region, as shown in Figure 1b, confirms that these nanoshells are mostly isolated, individual particles without

aggregation. The same area of the sample was also studied with confocal Raman microscopy, and a Raman intensity map (1435 cm^{-1} peak) is shown in Figure 1c. We can clearly observe strong Raman signals from individual Cu_2O nanoshells, as shown in this Raman map. The Raman intensity on each isolated nanoshell varies, largely due to the slight variation in the overall size, shell thickness, and porosity of these nanoshells.

Raman scattering on Cu_2O nanoshells with different Ostwald ripening times was further examined, which allowed exploration over the SERS sensitivity dependence on the structure and optical properties of the nanoshells. Extinction spectra of Cu_2O nanoshells with various ripening times are shown in Figure 1d. Due to the mesoscopic overall sizes of these nanoshells, their optical extinctions are dominated by scattering rather than absorption, and complex extinction spectral line-shapes are typically observed primarily due to phase retardation effects.^{31,35,36} Although these porous nanoshells are polycrystalline and composed of a large number of randomly oriented nanocrystals, the observed extinction line shapes and geometry-dependent tunability are apparently the synergistic optical characteristics of the mesoscopic Cu_2O nanoshells rather than the primary Cu_2O nanocrystals inside the shells. Detailed studies on such geometrically tunable optical properties of Cu_2O nanoshells have been reported elsewhere.^{31,36} Typical TEM images of the nanoshells are shown in Figure S1 in the Supporting Information, which show the progressive increase of shell porosity and the decrease of the shell thickness as the Ostwald ripening proceeds. We have measured SERS spectra of 4-ATP on these individual nanoshells obtained after varying

ripening times. Figures 1e and f show representative SERS spectra and the intensity histograms of the 1435 cm^{-1} peak, respectively. The SERS spectrum on individual Cu_2O nanoshells with 5 min of ripening shows very low Raman intensity, while significantly enhanced Raman signals are observed on the nanoshells obtained after 30 min of ripening. Ostwald ripening for 30 min introduced significant changes to the structure of the nanoshells, including decreased shell thickness and increased shell porosity. Such a porosity increase can enhance the adsorption of 4-ATP molecules on the surface of Cu_2O nanocrystals and may promote a more significant lightning rod effect at the junctions of the nanocrystals. In addition, such a structural change also shifts the Mie scattering resonance frequencies of these mesoscopic particles with respect to the excitation laser wavelength and alternates the profile of the extinction spectrum, resulting in enhanced scattering cross sections at the wavelength of the laser excitation (532 nm). All of these can be major reasons for the increase of the SERS signals.

The Raman scattering peaks, obtained on these porous Cu_2O nanoshells, appear at positions of 1004 , 1079 , 1141 , 1189 , 1389 , 1435 , and 1576 cm^{-1} , which are consistent with Raman spectra of adsorbed 4-ATP molecules.^{37–39} Among them, the peaks at 1141 , 1389 , and 1435 cm^{-1} were originally assigned to the b_2 modes due to the photoinduced charge transfer.¹⁷ Recently, it has also been reported that those peaks belong to the a_g modes of the DMAB molecules because of surface chemical transformation.^{40,41} While the origin of these peaks is still controversial, we observed that the SERS activities of the nanoshells decreased upon further ripening reactions as the extinction maximum was further blue-shifted to be off-resonance with the excitation laser. After Ostwald ripening for 120 min, the nanoshell structures collapsed when a thin-shell limit was reached. Due to the shell collapse, the unique optical tunability of the nanoshells was no longer maintained, and the collapsed shells exhibited extinction spectral features extremely similar to those of primary nanoparticles that are $\sim 15\text{--}30\text{ nm}$ in size. The SERS intensities obtained on these collapsed nanoshells turned out to be only about 16% of those from nanoshells obtained after 30 min of ripening. This is quite reasonable by considering the facts that the packing density of primary nanocrystals inside of each collapsed nanoshell becomes much lower (see TEM images in Figure S1 in the Supporting Information) and that there is a significant decrease of the scattering cross section at the excitation laser wavelength in comparison to that of the porous nanoshells. It is also possible that some changes in SERS intensities are related to the size of the primary nanoparticles because the size effect was recently reported for SERS enhancement on semiconductor substrates.¹⁶ Additional SERS experiments with different laser excitations can further clarify the effects of optical scattering and the particle size on overall SERS enhancement, and the results will be reported and discussed elsewhere.

Although Cu_2O nanocrystals ($15\text{--}30\text{ nm}$ in size) have small scattering cross sections at 532 nm (the wavelength of the laser excitation), we figured out that it was still possible to gain great SERS activities by hierarchically assembling Cu_2O nanocrystals into porous thin films. Here, we demonstrate that SERS-active substrates can be obtained by making porous thin films composed of Cu_2O nanoparticles via a Meyer rod coating technique. The Cu_2O nanoparticles were synthesized following a previously reported procedure.⁴² The as-synthesized Cu_2O nanoparticles dispersed in methanol give a yellow–orange

color, and the extinction spectrum (Figure 2a) shows two peaks at 352 and 452 nm , which are characteristic features of Cu_2O

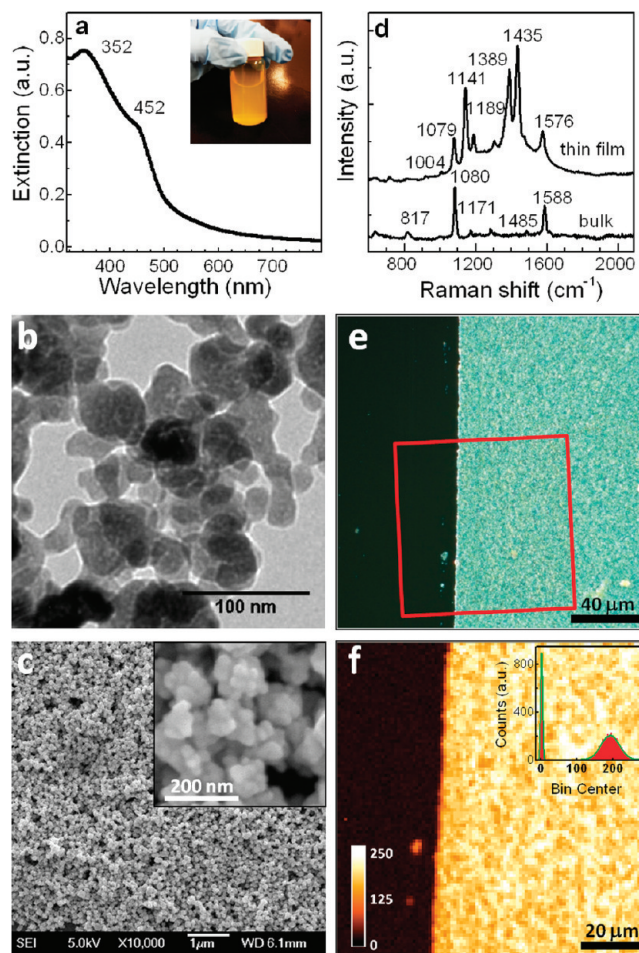


Figure 2. (a) Extinction spectrum of the as-synthesized Cu_2O nanoparticle dispersed in methanol. (Inset) Digital image of Cu_2O nanoparticle dispersion with yellowish color. (b) TEM micrograph of Cu_2O nanoparticle clusters. (c) Typical SEM images of the Cu_2O nanoparticle thin film; particle aggregation can be observed in the inset image with larger magnification. (d) Raman spectra of 4-ATP adsorbed on the Cu_2O nanoparticle thin film (top) and in the bulk powder state (bottom). (e) Dark-field optical image of the Cu_2O nanoparticle thin film with a prescratch on the left side. (f) Raman map of the area corresponding to the red box in (e). (Inset) Histogram of the Raman intensity.

nanoparticles with diameters of $15\text{--}30\text{ nm}$, as reported elsewhere.³² The overall spectral line shape is extremely similar to that of the collapsed nanoshells obtained after Ostwald ripening for 120 min. TEM measurements revealed irregular nanostructures, size distributions, and the agglomeration of Cu_2O nanoparticles in the porous thin films. As shown in Figure 2b, Cu_2O nanoparticles with an average size of $22.9 \pm 2.6\text{ nm}$ were hierarchically assembled into a porous structure with a number of nanometer-sized and even subnanometer-sized gaps. Additional results of TEM and X-ray diffraction (XRD) measurements can be found in the Supporting Information (Figures S2 and S3).

Uniform thin films composed of these nanoparticles with tunable thicknesses can be fabricated on a large scale using the Meyer rod coating method. Figure 2c shows a SEM image, which illustrates the overall morphology of the thin film over an

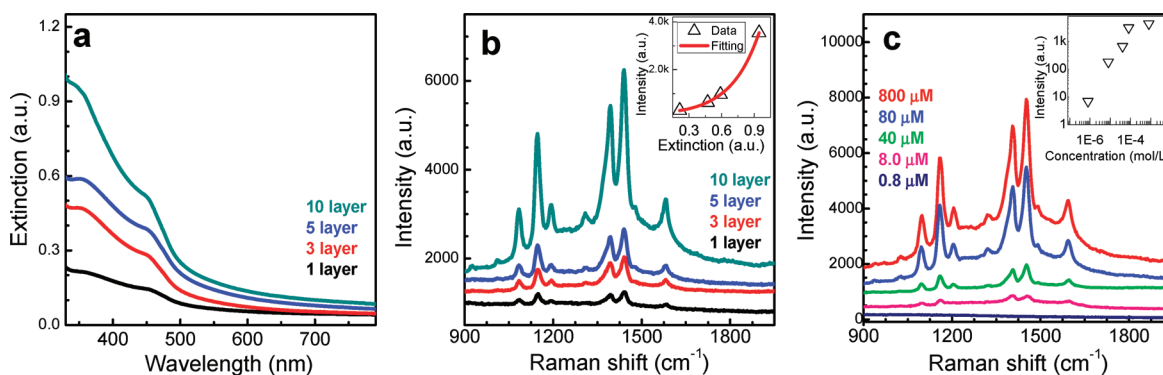


Figure 3. (a) Extinction spectra of Cu_2O thin films with tunable thicknesses via Meyer rod coating. (b) Raman spectra of 4-ATP ($800\ \mu\text{M}$) on Cu_2O nanoparticle thin films with different thicknesses. (Inset) Dependence of the Raman intensity on the film extinction. (c) Raman spectra of 4-ATP with variable concentration (from 0.8 to $800\ \mu\text{M}$). (Inset) The relationship between the Raman intensities at $1435\ \text{cm}^{-1}$ and the 4-ATP concentrations.

area of tens of micrometers. It is worth noting that nanoparticle aggregates with sizes around $100\ \text{nm}$ are observed, and these local aggregates result in porous structures in the thin films. A higher-magnification SEM image (shown as the inset of Figure 2c) clearly shows that each aggregate subdomain is composed of several primary nanoparticles with diameters in the range of $15\text{--}30\ \text{nm}$. Distinct Raman signals of probe molecules could be easily detected when we attached a monolayer of 4-ATP molecules onto the Cu_2O nanoparticle thin films. Figure 2d shows an enhanced Raman spectrum of 4-ATP molecules on a Cu_2O nanoparticle thin film that was immersed in $0.8\ \text{mM}$ 4-ATP for 3 h. The Raman spectrum of bulk 4-ATP powder is also shown for comparison. To ensure a monolayer adsorption of 4-ATP on the substrate, the Cu_2O nanoparticle thin-film substrate was washed thoroughly with DI water to remove the excessive 4-ATP molecules and then dried under a nitrogen stream before the Raman study. The enhanced Raman scattering could also be observed when crystal violet was used as the probe molecules (Figures S4 in the Supporting Information).

The Raman enhancement capability of Cu_2O nanoparticle thin films was also investigated via a combination of optical microscopy and confocal Raman map. Figures 2e and f reveal a dark-field optical image and a confocal Raman map of the 4-ATP-coated Cu_2O nanoparticle thin film, respectively. The thin film exhibits excellent uniformity and shows greenish-blue color under the dark-field microscopy. The confocal Raman map was utilized to obtain a SERS intensity distribution in the same area ($100 \times 100\ \mu\text{m}$, red box in the optical image). The Raman map is based on the intensity of 4-ATP peaks ranging from 890 to $1753\ \text{cm}^{-1}$. It is clearly revealed that the prescratched area showed almost no Raman signal, and uniform Raman intensity was observed from the area that was covered with Cu_2O nanoparticles. As shown in Figure 2f inset, SERS from the Cu_2O -nanoparticle-covered region has a normal distribution for their peak intensity with a relative standard deviation of 25%. We assume that such intensity deviation might be attributed to the various nanogaps between Cu_2O nanocrystals, which were observed in the SEM and TEM investigations.

A detailed evaluation of the SERS performance of Cu_2O porous thin films involves careful examinations of several important factors, such as the effects of film thickness on the overall SERS intensities, the concentration effects of the probe molecules, and the reproducibility of Raman enhancements at different sites on the films. The Meyer rod coating method

provides a convenient approach to fabricating large-area nanostructured thin films with tunable thickness and excellent uniformity.⁴³ As shown in Figure 3a, the extinction spectra of Cu_2O nanoparticle thin films shows an increased extinction with an increased deposition via the Meyer rod coating. With the increase of the extinction due to thickness increase, the line shape and peak positions of the extinction spectra are quite identical, indicating a uniform increase of film thickness while well-preserving the optical characteristics of the thin-film structures. Figure 3b shows the Raman spectra of 4-ATP adsorbed on the Cu_2O porous thin films with different thicknesses under green light ($532\ \text{nm}$, $0.88\ \text{mW}$) excitation. All of the peaks shown in the enhanced Raman spectra of 4-ATP are consistent with those in literature reports.^{37,38} The inset plot shows the relationship between the intensity of the Raman peak at $1435\ \text{cm}^{-1}$ and the intensity of extinction at $352\ \text{nm}$ of the thin films. It is clear that the Raman intensity increases dramatically with the increase of the Cu_2O film thickness. The curve fitting indicates that as the layer increases, the Raman intensity increases exponentially. The increase of the Raman intensity might be due to the increasing number and/or area of SERS "hot spots" in the nanoscale interparticle gaps as a consequence of the thicker layer of Cu_2O nanoparticle thin films. The Raman intensities for the porous thin films are quite uniform, as discussed previously in the confocal Raman scanning experiments.

We have further investigated Raman spectra of the probe molecules adsorbed on Cu_2O nanoparticle thin films that were immersed into 4-ATP solutions with different concentrations. The overall uniform SERS intensity on Cu_2O thin films allows a detailed exploration on adsorption of the probe molecules, which could be very critical for small molecules such as 4-ATP. Figure 3c shows the Raman spectra from the thin films with 4-ATP concentrations varied from 8×10^{-7} to $8 \times 10^{-4}\ \text{M}$. The Raman intensities are mostly linear when the 4-ATP concentrations are low, and the Raman intensities are saturated when the solution concentrations are high. This result agrees with the model of Langmuir adsorption that has been discussed in detail by others.⁴⁴ We could clearly observe 4-ATP Raman signals when a solution with a concentration as low as $8\ \mu\text{M}$ was used.

We estimated the SERS enhancement factor (EF) on the porous Cu_2O nanoparticle thin films to be around 35 000 based on the known method.^{6,45} The SERS EF on nanoshells with a 30 min ripening process are estimated to be about an order of

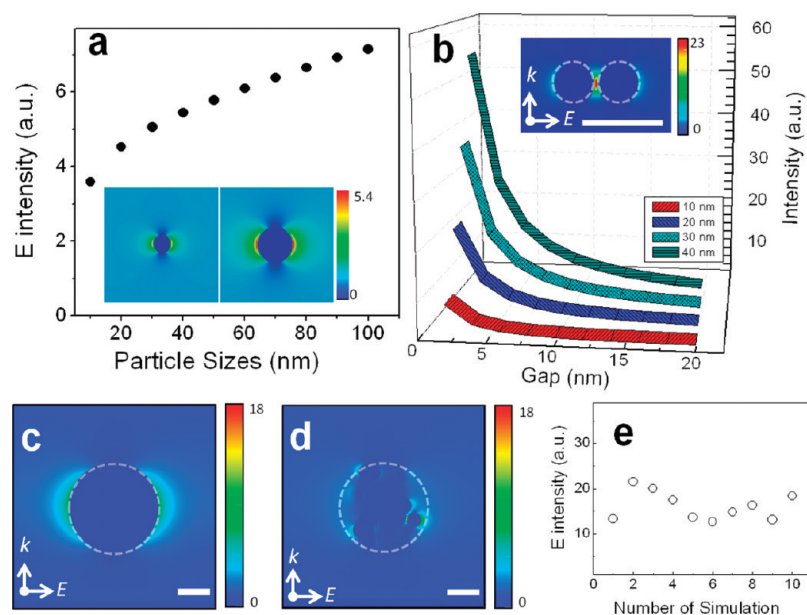


Figure 4. FDTD simulations of the scattering-enhanced electric field: (a) electric field intensity as a function of the size of Cu_2O nanoparticles; (inset) electric field intensity of individual Cu_2O nanoparticles of 20 and 40 nm; (b) gap dependence of the intensities of the electric field enhanced by two nanocrystals; (inset) two Cu_2O nanoparticles (20 nm in diameter) with a gap of 2 nm; (c) FDTD simulation of a solid Cu_2O nanosphere; (d) FDTD simulation of a porous Cu_2O nanoparticle; (e) variation of the electric field intensity maximum in porous nanoparticle aggregates. The scale bars are 40 nm for all of the panels.

magnitude higher than that achievable on porous thin films if we assume that the SERS enhancements on the porous Cu_2O nanoshells and those on the collapsed nanoshells are similar due to their structural and optical similarity. We attribute the Raman enhancement to a combination of scattering-induced electromagnetic field enhancement and chemical enhancement due to adsorption of 4-ATP to Cu_2O nanostructures. We have also assembled Cu_2O micrometer-sized polyhedral particles into thin films. Under similar condition (8×10^{-4} M 4-ATP solution treatment), however, we detected extremely weak Raman scattering from the thin films of micrometer-sized particles (Figures S5 in the Supporting Information). It is highly likely that micrometer-sized Cu_2O particles have a relatively small surface area available for the adsorption of 4-ATP and lack the porous hierarchical structures possessing a large number of nanoscale interparticle gaps that may be crucial for the local electromagnetic field enhancement.

Our experimental results can be further understood when correlated with a FDTD simulation. FDTD is one of the primary available computational electrodynamic modeling techniques, which can be applied to predicting near-field electromagnetic (EM) distributions in the vicinity of an optical scatter. We have conducted a series of computations to understand the effects of hierarchical assembly of Cu_2O nanoparticle clusters on the local EM field enhancement. Figure 4a shows the size effect of Cu_2O nanoparticles on the enhancement of the localized electromagnetic field. To more quantitatively illustrate the local EM enhancement inside of the nanoscale interparticle junctions, we performed FDTD simulation on Cu_2O nanoparticle homodimers that are composed of two identical nanospheres in close proximity to each other. As shown in Figure 4b, the local EM field is significantly enhanced when the interparticle gap is small in comparison to the particle size. A total EM enhancement of around 22 can be obtained for the hot spot between the 20 nm particles with a gap of 2 nm (Figure 4b, inset). For 40 nm

particles, the electric field enhancements can be as high as 56. Because Cu_2O is a semiconductor and its plasmon resonances are not in the visible region, we believe such EM enhancement can be a result of the lightning rod effect, which was found to be very significant for hierarchically assembled porous nanostructures in comparison to that of individual solid particles. As shown in Figure 4c and d, the porous Cu_2O nanoparticle cluster has multiple spots with high EM intensity due to the porous structures and nanoscale interparticle gaps. The maximum EM intensity achievable inside of the porous nanoparticle aggregate (Figure 4d) is 16.37, which is more than double as compared to that of a solid Cu_2O sphere with a similar overall size (Figure 4c). We have constructed 10 porous nanoparticle aggregates and found that the simulated results were quite reproducible (Figure 4e).

On the basis of both the experimental and computational results, the observed Raman enhancement of the probe molecules on the hierarchical porous Cu_2O nanostructures can be most reasonably described as a result of the synergistic effect of strong chemical interactions between molecules and cuprous oxide surfaces, localized electromagnetic field enhancement, and the unique hierarchical porosity of the nanostructures. With the recent study of SERS on semiconductor substrates, there are plenty of reports on the strong chemical interactions between probe molecules and semiconductors.⁴⁶ Because the thiol groups have strong affinity for transition metals, we believe that in our case, 4-ATP can be strongly adsorbed on Cu_2O nanoparticles. Such adsorption will possibly induce charge transfer between the 4-ATP molecules and Cu_2O nanoparticles and consequently enhance the Raman signals. On the other hand, Cu_2O can also act as a surface catalyst that promotes the molecular dimerization of 4-ATP to form DMAB, which has a larger Raman cross section and a different way of interacting with the Cu_2O surface to generate even stronger Raman signals. In either mechanism, the chemical enhancement of 4-ATP on the surface of Cu_2O nanocrystals is undoubtedly

demonstrated. Besides the chemical enhancement, electromagnetic enhancement can be another major reason for the strong Raman enhancements. Our preliminary FDTD simulation indicates that the local EM is easily enhanced by 4–8 times near individual Cu₂O nanoparticles with a size of 20–100 nm, while hot spots with much higher EM intensity can be obtained on hierarchically assembled nanoparticle aggregates. Although larger particles can result in a stronger local EM field, as predicted by FDTD calculations, we did not observe strong Raman enhancement on micrometer-sized Cu₂O polyhedral particles. This can be related to the relatively small surface area accessible for molecular adsorption and the lack of enough hot spots for the large particles. It is noteworthy that the porous polycrystalline nanoshells and thin films provide an excellent opportunity for both chemical enhancement (due to the large surface area and molecule–surface interactions) and physical enhancement (with plenty of hot spots) to contribute to the overall Raman enhancement. All of these factors work concurrently and make the Cu₂O porous nanostructures reported here a unique type of substrates with reproducible Raman EFs on the order of 10⁴–10⁵. This is a larger Raman enhancement as compared to that of other semiconductor SERS substrates reported earlier, such as the TiO₂ nanostructures on which no EM enhancement was observed.¹⁶ Our work presents, for the first time, a systematic study of the Raman enhancement on hierarchical porous Cu₂O nanostructures and opens up new opportunities of probing interesting physical and chemical processes that may occur on Cu₂O surfaces by SERS.

■ ASSOCIATED CONTENT

Supporting Information

Experimental details including syntheses of Cu₂O nanoparticles and the fabrication of porous Cu₂O thin films, additional sample characterizations, SERS spectra of crystal violet, SEM image of Cu₂O microparticles, and details for FDTD simulation. This material is available free of charge via the Internet at <http://pubs.acs.org>.

■ AUTHOR INFORMATION

Corresponding Author

*E-mail: wang344@mailbox.sc.edu (H.W.); chaoyang.jiang@usd.edu (C.J.).

Notes

The authors declare no competing financial interest.

■ ACKNOWLEDGMENTS

C.J. would like to acknowledge the support by the National Science Foundation/EPSCoR Grant No. 0903804, by NASA (Cooperative Agreement Number: NNX10AN34A), and by the State of South Dakota. We are also thankful for support from NSF CHE-0722632 and CHE-0840507. Parts of this work were carried out in the Characterization Facility, University of Minnesota, which receives partial support from NSF through the MRSEC Program DMR-0819885. We thank Mr. Rui Peng and Dr. Ranjit Koodali for XRD experiments and Dr. Ozan Ugurlu, Dr. Bing Luo, and Dr. John Nelson for nanocrystal characterization and valuable discussion. H.W. would like to acknowledge the College of Arts and Sciences of the University of South Carolina for generous start-up support and the USC Electron Microscopy Center for instrument use and scientific and technical assistance.

■ REFERENCES

- (1) Jeanmaire, D. L.; Van Duyne, R. P. Surface Raman Spectroelectrochemistry: Part I. Heterocyclic, Aromatic, and Aliphatic Amines Adsorbed on the Anodized Silver Electrode. *J. Electroanal. Chem. Interfacial Electrochem.* **1977**, *84*, 1–20.
- (2) Albrecht, M. G.; Creighton, J. A. Anomalous Intense Raman Spectra of Pyridine at a Silver Electrode. *J. Am. Chem. Soc.* **1977**, *99*, 5215–5217.
- (3) Haes, A. J.; Haynes, C. L.; McFarland, A. D.; Schatz, G. C.; Van Duyne, R. R.; Zou, S. L. Plasmonic Materials for Surface-Enhanced Sensing and Spectroscopy. *MRS Bull.* **2005**, *30*, 368–375.
- (4) Kneipp, J.; Kneipp, H.; Kneipp, K. SERS — A Single-Molecule and Nanoscale Tool for Bioanalytics. *Chem. Soc. Rev.* **2008**, *37*, 1052–1060.
- (5) Li, J. F.; Huang, Y. F.; Ding, Y.; Yang, Z. L.; Li, S. B.; Zhou, X. S.; Fan, F. R.; Zhang, W.; Zhou, Z. Y.; Wu, D. Y.; et al. Shell-Isolated Nanoparticle-Enhanced Raman Spectroscopy. *Nature* **2010**, *464*, 392–395.
- (6) Kumar, J.; Thomas, K. G. Surface-Enhanced Raman Spectroscopy: Investigations at the Nanorod Edges and Dimer Junctions. *J. Phys. Chem. Lett.* **2011**, *2*, 610–615.
- (7) Banholzer, M. J.; Millstone, J. E.; Qin, L. D.; Mirkin, C. A. Rationally Designed Nanostructures for Surface-Enhanced Raman Spectroscopy. *Chem. Soc. Rev.* **2008**, *37*, 885–897.
- (8) Chen, T.; Wang, H.; Chen, G.; Wang, Y.; Feng, Y. H.; Teo, W. S.; Wu, T.; Chen, H. Y. Hotspot-Induced Transformation of Surface-Enhanced Raman Scattering Fingerprints. *ACS Nano* **2010**, *4*, 3087–3094.
- (9) Lal, S.; Grady, N. K.; Kundu, J.; Levin, C. S.; Lassiter, J. B.; Halas, N. J. Tailoring Plasmonic Substrates for Surface Enhanced Spectroscopies. *Chem. Soc. Rev.* **2008**, *37*, 898–911.
- (10) Halas, N. J.; Lal, S.; Chang, W.-S.; Link, S.; Nordlander, P. Plasmons in Strongly Coupled Metallic Nanostructures. *Chem. Rev.* **2011**, *111*, 3913–3961.
- (11) Alvarez-Puebla, R. A.; Agarwal, A.; Manna, P.; Khanal, B. P.; Aldeanueva-Potel, P.; Carbo-Argibay, E.; Pazos-Perez, N.; Vigdeman, L.; Zubarev, E. R.; Kotov, N. A.; et al. Gold Nanorods 3d-Supercrystals as Surface-Enhanced Raman Scattering Spectroscopy Substrates for the Rapid Detection of Scrambled Prions. *Proc. Natl. Acad. Sci. U.S.A.* **2011**, *108*, 8157–8161.
- (12) Kattumenu, R.; Lee, C. H.; Tian, L.; McConney, M. E.; Singamaneni, S. Nanorod Decorated Nanowires as Highly Efficient SERS-Active Hybrids. *J. Mater. Chem.* **2011**, *21*, 15218–15223.
- (13) Jones, M. R.; Osberg, K. D.; Macfarlane, R. J.; Langille, M. R.; Mirkin, C. A. Templated Techniques for the Synthesis and Assembly of Plasmonic Nanostructures. *Chem. Rev.* **2011**, *111*, 3736–3827.
- (14) Tian, Z. Q.; Ren, B.; Wu, D. Y. Surface-Enhanced Raman Scattering: From Noble to Transition Metals and from Rough Surfaces to Ordered Nanostructures. *J. Phys. Chem. B* **2002**, *106*, 9463–9483.
- (15) Quagliano, L. G. Observation of Molecules Adsorbed on III–V Semiconductor Quantum Dots by Surface-Enhanced Raman Scattering. *J. Am. Chem. Soc.* **2004**, *126*, 7393–7398.
- (16) Musumeci, A.; Gosztola, D.; Schiller, T.; Dimitrijevic, N. M.; Mujica, V.; Martin, D.; Rajh, T. SERS of Semiconducting Nanoparticles (TiO₂ Hybrid Composites). *J. Am. Chem. Soc.* **2009**, *131*, 6040–6041.
- (17) Wang, X. T.; Shi, W. S.; She, G. W.; Mu, L. X. Using Si and Ge Nanostructures as Substrates for Surface-Enhanced Raman Scattering Based on Photoinduced Charge Transfer Mechanism. *J. Am. Chem. Soc.* **2011**, *133*, 16518–16523.
- (18) Tarakeshwar, P.; Finkelstein-Shapiro, D.; Hurst, S. J.; Rajh, T.; Mujica, V. Surface-Enhanced Raman Scattering on Semiconducting Oxide Nanoparticles: Oxide Nature, Size, Solvent, and pH Effects. *J. Phys. Chem. C* **2011**, *115*, 8994–9004.
- (19) Rai, B. P. Cu₂O Solar Cells: A Review. *Sol. Cells* **1988**, *25*, 265–272.
- (20) Yang, L.; Luo, S.; Li, Y.; Xiao, Y.; Kang, Q.; Cai, Q. High Efficient Photocatalytic Degradation of *p*-Nitrophenol on a Unique

Cu₂O/TiO₂ P–N Heterojunction Network Catalyst. *Environ. Sci. Technol.* **2010**, *44*, 7641–7646.

(21) Xu, L.; Jiang, L.-P.; Zhu, J.-J. Sonochemical Synthesis and Photocatalysis of Porous Cu₂O Nanospheres with Controllable Structures. *Nanotechnology* **2009**, *20*, 045605.

(22) Jang, H. S.; Kim, S. J.; Choi, K.-S. Construction of Cuprous Oxide Electrodes Composed of 2D Single-Crystalline Dendritic Nanosheets. *Small* **2010**, *6*, 2183–2190.

(23) Park, J. C.; Kim, J.; Kwon, H.; Song, H. Gram-Scale Synthesis of Cu₂O Nanocubes and Subsequent Oxidation to CuO Hollow Nanostructures for Lithium-Ion Battery Anode Materials. *Adv. Mater.* **2009**, *21*, 803–807.

(24) Huang, L.; Peng, F.; Yu, H.; Wang, H. J. Synthesis of Cu₂O Nanoboxes, Nanocubes and Nanospheres by Polyol Process and Their Adsorption Characteristic. *Mater. Res. Bull.* **2008**, *43*, 3047–3053.

(25) Zhang, J.; Liu, J.; Peng, Q.; Wang, X.; Li, Y. Nearly Monodisperse Cu₂O and CuO Nanospheres: Preparation and Applications for Sensitive Gas Sensors. *Chem. Mater.* **2006**, *18*, 867–871.

(26) Yin, M.; Wu, C.-K.; Lou, Y.; Burda, C.; Koberstein, J. T.; Zhu, Y.; O'Brien, S. Copper Oxide Nanocrystals. *J. Am. Chem. Soc.* **2005**, *127*, 9506–9511.

(27) Gou, L.; Murphy, C. J. Solution-Phase Synthesis of Cu₂O Nanocubes. *Nano Lett.* **2003**, *3*, 231–234.

(28) Wang, Z.; Wang, H.; Wang, L.; Pan, L. Controlled Synthesis of Cu₂O Cubic and Octahedral Nano- and Microcrystals. *Cryst. Res. Technol.* **2009**, *44*, 624–628.

(29) Kuo, C. H.; Huang, M. H. Morphologically Controlled Synthesis of Cu₂O Nanocrystals and Their Properties. *Nano Today* **2010**, *5*, 106–116.

(30) Huang, W. X.; Bao, H. Z.; Zhang, W. H.; Shang, D. L.; Hua, Q.; Ma, Y. S.; Jiang, Z. Q.; Yang, J. L. Shape-Dependent Reducibility of Cuprous Oxide Nanocrystals. *J. Phys. Chem. C* **2010**, *114*, 6676–6680.

(31) Zhang, L.; Wang, H. Cuprous Oxide Nanoshells with Geometrically Tunable Optical Properties. *ACS Nano* **2011**, *5*, 3257–3267.

(32) Bardhan, R.; Grady, N. K.; Ali, T.; Halas, N. J. Metallic Nanoshells with Semiconductor Cores: Optical Characteristics Modified by Core Medium Properties. *ACS Nano* **2010**, *4*, 6169–6179.

(33) Kudelski, A.; Grochala, W.; Janik-Czachor, M.; Bukowska, J.; Szumner, A.; Dolata, M. Surface-Enhanced Raman Scattering (SERS) at Copper(I) Oxide. *J. Raman Spectrosc.* **1998**, *29*, 431–435.

(34) Wang, Y.-X.; Song, W.; Yang, J.-X.; Xu, W.-Q.; Zhao, B. Surface Enhanced Raman Scattering on Cu₂O/Ag Composite. *Chem. J. Chin. Univ.* **2011**, *32*, 1789–1793.

(35) Bohren, C. F.; Huffman, D. R., *Absorption and Scattering of Light by Small Particles*; John Wiley & Sons: New York: 1998.

(36) Zhang, L.; Wang, H. Interior Structural Tailoring of Cu₂O Shell-in-Shell Nanostructures through Multistep Ostwald Ripening. *J. Phys. Chem. C* **2011**, *115*, 18479–18485.

(37) Wang, E. K.; Guo, S. J.; Dong, S. J. Rectangular Silver Nanorods: Controlled Preparation, Liquid–Liquid Interface Assembly, and Application in Surface-Enhanced Raman Scattering. *Cryst. Growth Des.* **2009**, *9*, 372–377.

(38) Dong, S. J.; Hu, X. G.; Wang, T.; Wang, L. Surface-Enhanced Raman Scattering of 4-Aminothiophenol Self-Assembled Monolayers in Sandwich Structure with Nanoparticle Shape Dependence: Off-Surface Plasmon Resonance Condition. *J. Phys. Chem. C* **2007**, *111*, 6962–6969.

(39) Mao, Z.; Song, W.; Chen, L.; Ji, W.; Xue, X.; Ruan, W.; Li, Z.; Mao, H.; Ma, S.; Lombardi, J. R.; et al. Metal–Semiconductor Contacts Induce the Charge-Transfer Mechanism of Surface-Enhanced Raman Scattering. *J. Phys. Chem. C* **2011**, *115*, 18378–18383.

(40) Huang, Y.-F.; Zhu, H.-P.; Liu, G.-K.; Wu, D.-Y.; Ren, B.; Tian, Z.-Q. When the Signal Is Not from the Original Molecule to Be Detected: Chemical Transformation of *para*-Aminothiophenol on Ag during the SERS Measurement. *J. Am. Chem. Soc.* **2010**, *132*, 9244–9246.

(41) Dong, B.; Fang, Y. R.; Chen, X. W.; Xu, H. X.; Sun, M. T. Substrate-, Wavelength-, and Time-Dependent Plasmon-Assisted Surface Catalysis Reaction of 4-Nitrobenzenethiol Dimerizing to *p,p'*-Dimercaptoazobenzene on Au, Ag, and Cu Films. *Langmuir* **2011**, *27*, 10677–10682.

(42) Zhang, D.-F.; Zhang, H.; Guo, L.; Zheng, K.; Han, X.-D.; Zhang, Z. Delicate Control of Crystallographic Facet-Oriented Cu₂O Nanocrystals and the Correlated Adsorption Ability. *J. Mater. Chem.* **2009**, *19*, 5220–5225.

(43) Hu, L.; Kim, H. S.; Lee, J.-Y.; Peumans, P.; Cui, Y. Scalable Coating and Properties of Transparent, Flexible, Silver Nanowire Electrodes. *ACS Nano* **2010**, *4*, 2955–2963.

(44) Tao, A.; Kim, F.; Hess, C.; Goldberger, J.; He, R. R.; Sun, Y. G.; Xia, Y. N.; Yang, P. D. Langmuir–Blodgett Silver Nanowire Monolayers for Molecular Sensing Using Surface-Enhanced Raman Spectroscopy. *Nano Lett.* **2003**, *3*, 1229–1233.

(45) Hong, G.; Li, C.; Limin, Q. Facile Fabrication of Two-Dimensionally Ordered Macroporous Silver Thin Films and Their Application in Molecular Sensing. *Adv. Funct. Mater.* **2010**, *20*, 3774–3783.

(46) Hurst, S. J.; Fry, H. C.; Gosztola, D. J.; Rajh, T. Utilizing Chemical Raman Enhancement: A Route for Metal Oxide Support-Based Biodetection. *J. Phys. Chem. C* **2011**, *115*, 620–630.

Surface-Enhanced Raman Scattering on Hierarchical Porous Cuprous Oxide Nanostructures in Nanoshell and Thin Film Geometries

Chao Qiu,[†] Li Zhang,[‡] Hui Wang,^{‡,} and Chaoyang Jiang^{†,*}*

[†] Department of Chemistry, University of South Dakota, Vermillion, South Dakota 57069, United States

[‡] Department of Chemistry and Biochemistry, University of South Carolina, Columbia, South Carolina 29208, United States

Supporting Information

Methods

Syntheses of Cu₂O nanoparticles: The Cu₂O nanoparticles were synthesized according to a previously reported method.¹ All chemicals reagents for nanocrystal syntheses were analytical grade and were used without any further purification. In a typical synthesis, 3.333 g polyvinylpyrrolidone (PVP, Mw=1,300,000, Alfa) was dissolved in CuCl₂ (0.01mol/L, 100 ml) aqueous solution. Then, 10 mL NaOH (2.0 mol/L) solution was added dropwise into above transparent light green solution. During this process, the color of the solution was changed to turbid blue-green, and then to dark brown. After stirring for 0.5 h., an ascorbic solution (10 mL, 0.60 mol/L) was added dropwise into the dark brown solution. The mixture was aged at room temperature under constant stirring for three hours and the final solution changed to orange-yellow. After the reaction, centrifugation was used for several times to remove the residual inorganic ions and polymer. The final product was dispersed in methanol with a volume of 40

mL. Some products after purification were dried in vacuum at 50 °C for further characterization. For the synthesis of Cu₂O micro particles, we have followed a method reported elsewhere² and D-glucose was used in the reaction. The size of Cu₂O particles was determined by SEM measurements and the products have been repeated several times in our experiments.

Thin film preparation: The Meyer rod coating was employed to fabricate scalable and uniform Cu₂O nanoparticle thin films. The glass substrate is put on a flat plate and a Meyer rod was pulled over the ink and substrate, which leaves a uniform layer of Cu₂O nanoparticles. The thicknesses of the thin films can be controlled by repeating the coating process. For enhanced Raman measurements, the well prepared Cu₂O nanoparticle thin films were incubated in 4-aminothiophenol (4-ATP) and crystal violet (CV) solutions for three hours, respectively, a similar procedure as being reported by others.^{3, 4} The samples were then thoroughly washed using ethanol. This typical incubate-wash treatment could assure to get rid of the excess molecules on the surface. The Cu₂O thin films were then washed thoroughly using DI-water and dried under N₂ before the spectroscopic study.

Characterization: X-Ray powder diffraction (XRD, Rigaku Ultima IV diffractometer) was employed for crystal structure determination. Absorbance spectra were carried out on a Cary 50 UV-Vis spectrophotometer. Furthermore, the microstructures were analyzed by using transmission electron microscopy (TEM) on a FEI Tecnai electron microscope with an acceleration voltage of 120 kV. Scanning electron microscopy (SEM) was used for the examination of the morphologies of Cu₂O nanoparticle thin films. SEM micrographs were obtained on a Zeiss Supra40VP variable-pressure field-emission SEM. All SERS spectra and confocal Raman images were collected on an Aramis confocal microscope (Horiba Jobin Yvon, Edison, NJ) equipped with a diode-pump solid state (DSPP) laser (532 nm). The laser, with an intensity of 0.88 mW, was focused using a 50× objective (NA 0.75) onto the samples on the glass slides, which were mounted onto a 200×200×200 μm piezo scanner. The Raman signals were collected with the same objective under a 180° back-scattering configuration and passed through an edge filter into a monochromator and electric-cooled charge-coupled devices (CCD) camera. To obtain a Raman map, an array of Raman spectra was collected when the laser was raster scanned across a selected area of the sample. The Raman spectra were acquired for 1 s at each pixel. The spectra were then mathematically processed, and the intensity distribution for the Raman peaks of interest can be revealed.

Experimental results

TEM images of polycrystalline nanoshells are shown in Figure S1, where the porosity changes during the Ostwald ripening process can be clearly observed. This result is consistent with what has been reported previously.⁵

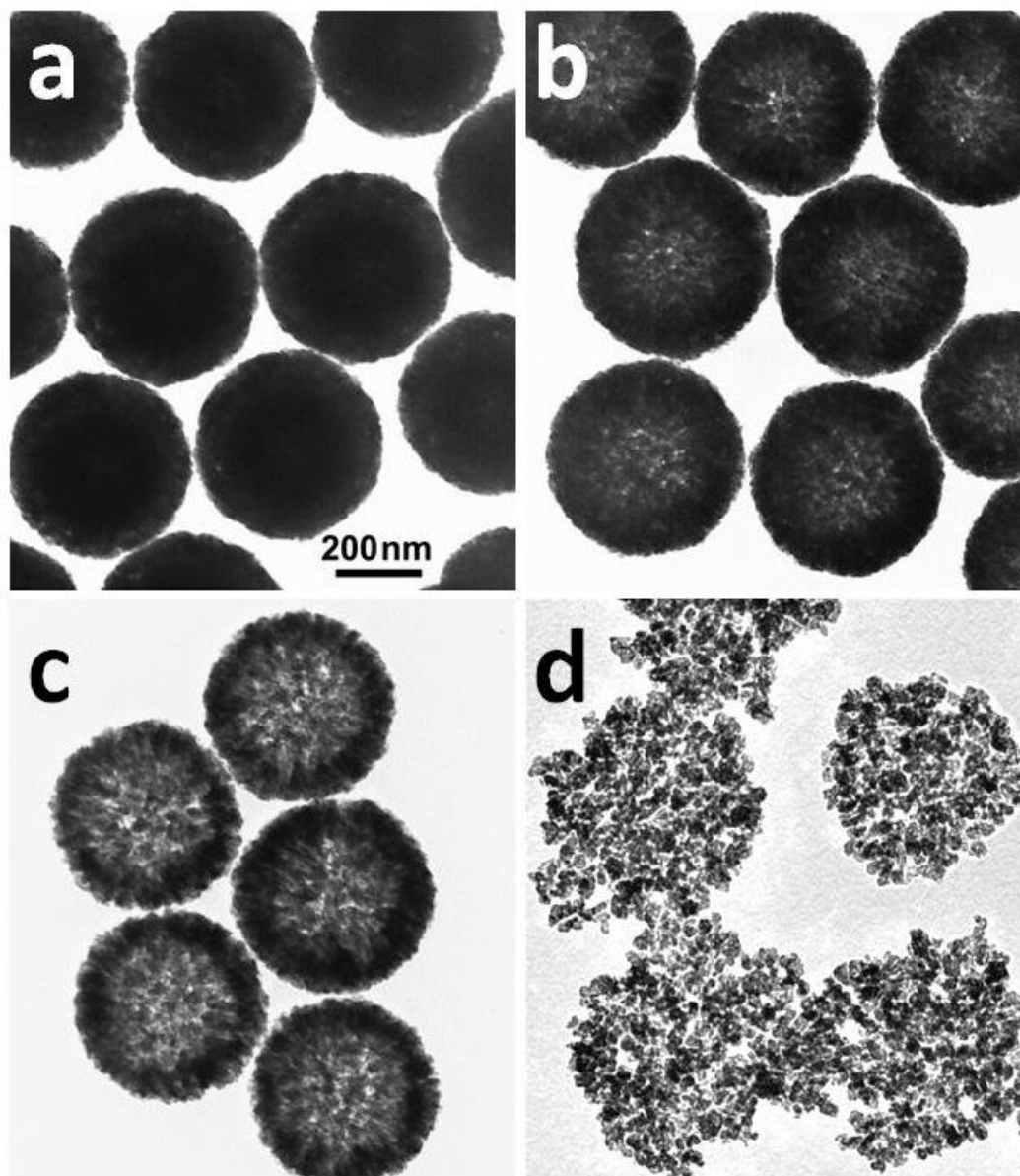


Figure S1. TEM images of nanoshells obtained after Ostwald ripening for (a) 5 minutes; (b) 30 minutes; (c) 60 minutes; and (d) 120 minutes.

TEM measurements of Cu_2O nanoparticles revealed irregular nanoscale structures, size distributions, and the agglomeration of Cu_2O nanoparticles. As shown in Figure S2a, the Cu_2O

nanoparticles with size below 40 nm were aggregated in a porous manner, which is very similar to that of SEM observations. The size distribution of nanoparticles was obtained as shown in the inset of Figure S2a where about 150 nanoparticles were measured and the histogram shows a normal distribution with an average size of 22.9 ± 2.6 nm. Figure S2b gives a HRTEM image of a Cu_2O nanoparticle which clearly indicates the crystal lattice structure. The lattice plane distance is 3.0 \AA , which can be assigned to the d space of (110) planes for cubic phase Cu_2O crystals. The corresponding fast Fourier transform pattern of the HRTEM image is shown in the Figure S2b inset, indicating a highly crystalline quality of Cu_2O nanoparticles.

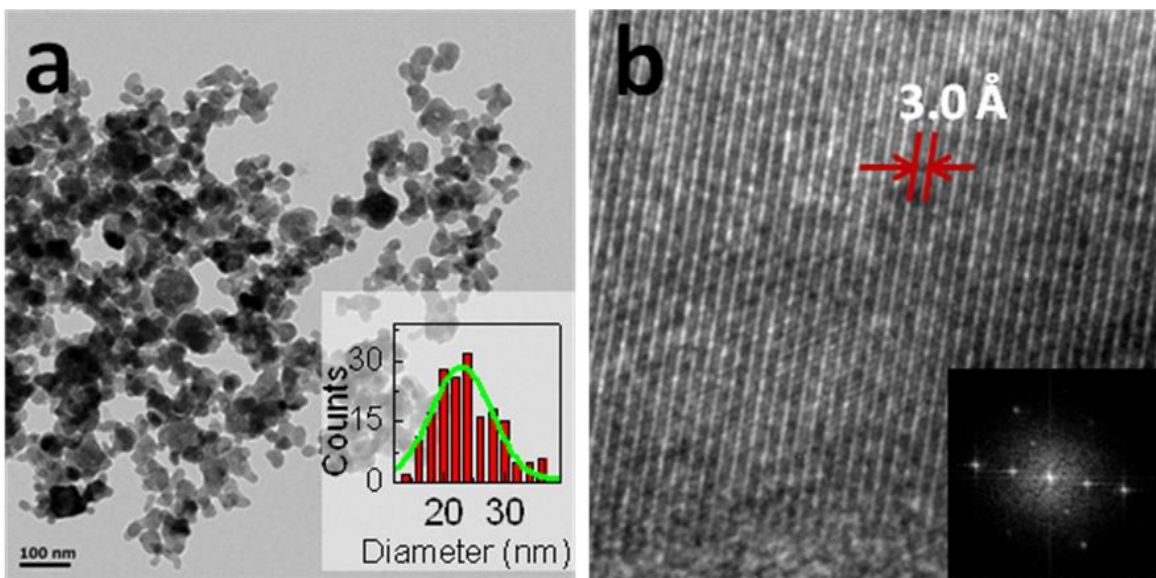


Figure S2. a. TEM micrograph of Cu_2O nanoparticle aggregations, inset: size distribution of Cu_2O nanoparticles; b. HRTEM image of a Cu_2O nanoparticle with high crystallinity, inset: corresponding fast Fourier transfer image.

The Cu_2O crystal structure was further confirmed by X-ray powder diffraction (XRD) and Raman spectroscopy. Figure S3a exhibits the XRD pattern of as-prepared Cu_2O nanoparticles. We notice that all of the peaks have well agreed with Bragg reflections of the standard cubic cuprite structure (Pn3m $a = 4.267 \text{ \AA}$ PDF card No.078-2076). Such XRD results confirmed the purity of our Cu_2O crystalline structures and indicated that there are no detectable crystalline structures of any contaminations. The Cu_2O nanoparticle crystal structure was further confirmed by Raman spectroscopy (Figure S3b). Three sharp Raman shift peaks at 96, 151, 220 cm^{-1} can be observed, and these peaks match perfectly with literature reports.⁶

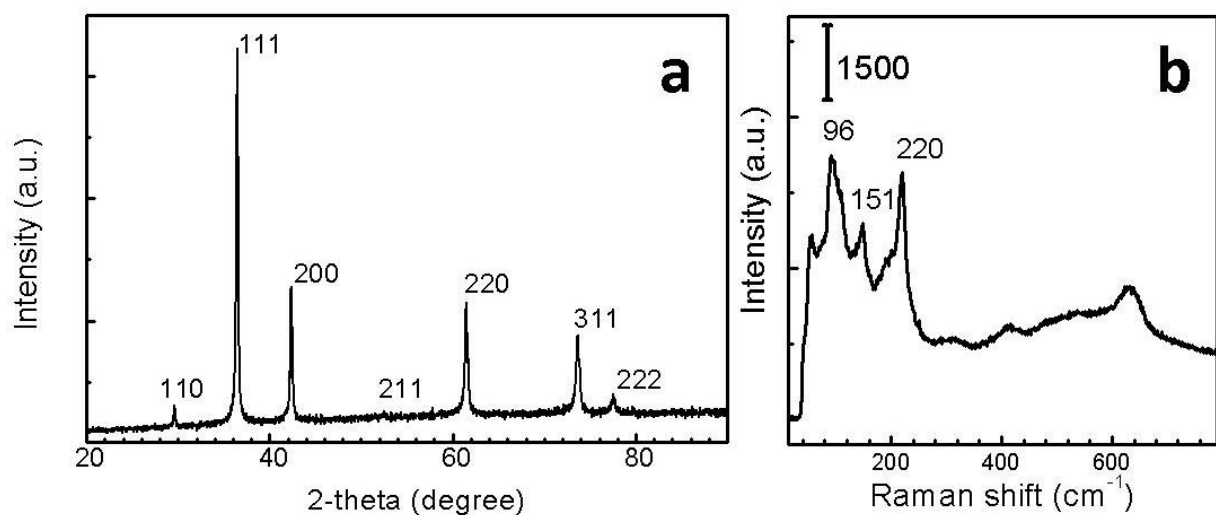


Figure S3. a, XRD pattern of the as-synthesized Cu₂O nanoparticles; b, typical Raman spectrum of Cu₂O nanoparticle thin film.

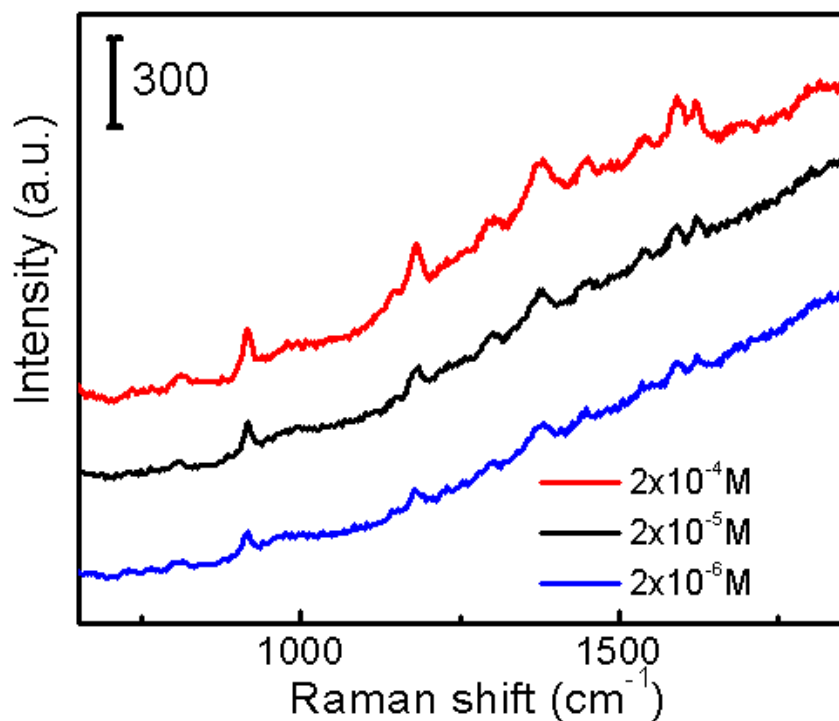


Figure S4. Enhanced Raman spectra of crystal violet (CV) obtained on Cu₂O nanoparticle thin films that were incubated with CV solutions of different concentrations.

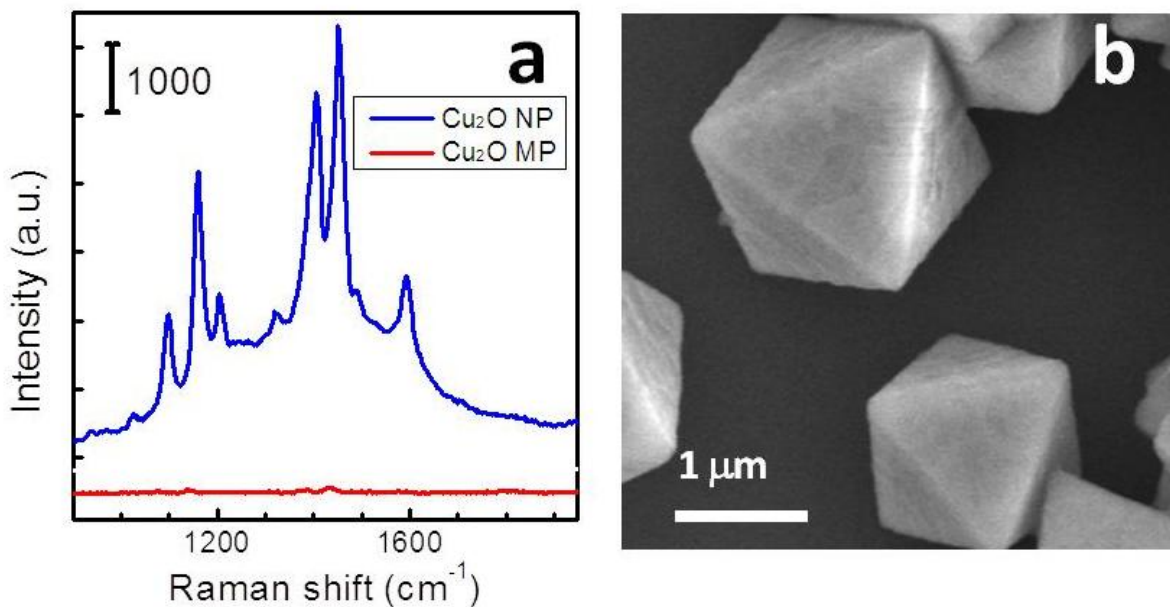


Figure S5. a, Raman spectra of 4-ATP in the same concentration (0.8 mM) with different substrates, Cu₂O nanoparticle thin film and Cu₂O micro particle thin film; b, SEM image of the Cu₂O micro particle used in the Raman measurement in a.

FDTD simulation

Theoretical simulation of the near-field electro-magnetic intensity was conducted via a Finite-difference time-domain (FDTD) approach by using EM Explorer software. The optical constants of cuprous oxide ($n = 3.113$, $k = 0.232$, with an irradiation of 532 nm light) are obtained from SOPRA N&K Database. A 128 nm grid size and 1.0 nm Yee cell were used in our calculations for single Cu₂O particle simulation. The porous nanoparticle aggregates in the simulations were constructed by 200 Cu₂O nanocrystals (20 nm in diameter) randomly distributed within a large sphere of 114 nm (the average size of particle aggregations). 256 nm grid size and 1.0 nm Yee cell were used in the simulation. We have done multiple simulations on porous nanoparticle aggregates and two examples are shown in Figure S6. The results were processed with ParaView software for visualization.

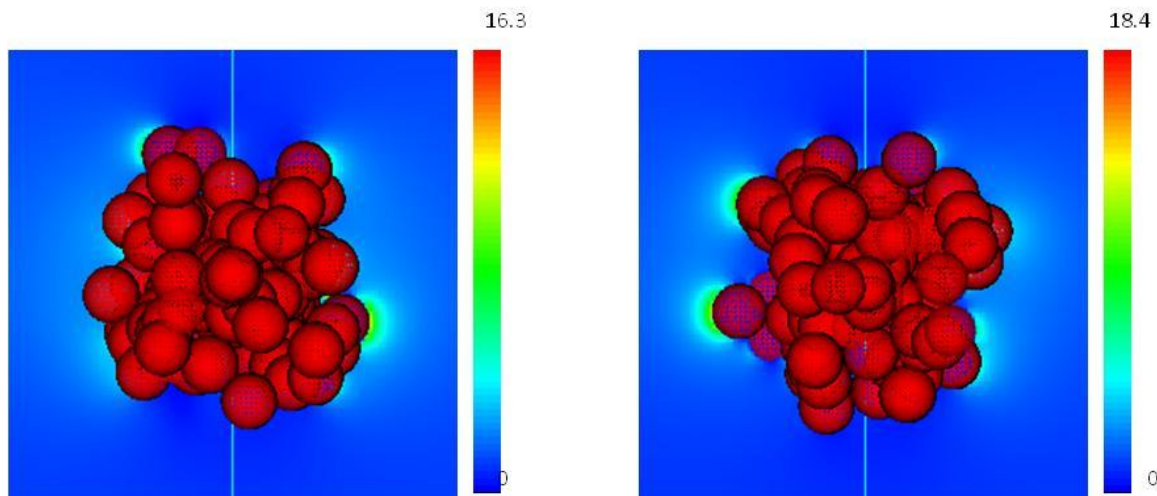


Figure S6. Typical two examples of porous nanoparticle aggregates that were simulated. The red color on the small particles is generated during the three dimensional construction rather than represent the EM intensity.

References

- S1. Zhang, D.-F.; Zhang, H.; Guo, L.; Zheng, K.; Han, X.-D.; Zhang, Z., Delicate Control of Crystallographic Facet-Oriented Cu_2O Nanocrystals and the Correlated Adsorption Ability. *J. Mater. Chem.* **2009**, *19*, 5220-5225.
- S2. Yang, Z.; Sun, S.; Kong, C.; Song, X.; Ding, B., Designated-Tailoring on {100} Facets of Cu_2O Nanostructures: From Octahedral to Its Different Truncated Forms. *Journal of Nanomaterials* **2010**, *2010*, 710584.
- S3. Ponce, I.; Silva, J. F.; Onate, R.; Miranda-Rojas, S.; Munoz-Castro, A.; Arratia-Perez, R.; Mendizabal, F.; Zagal, J. H., Theoretical and Experimental Study of Bonding and Optical Properties of Self-Assembly Metallophthalocyanines Complexes on a Gold Surface. A Survey of the Substrate-Surface Interaction. *J. Phys. Chem. C* **2011**, *115*, 23512-23518.
- S4. Hong, G. S.; Li, C.; Qi, L. M., Facile Fabrication of Two-Dimensionally Ordered Macroporous Silver Thin Films and Their Application in Molecular Sensing. *Adv. Funct. Mater.* **2010**, *20*, 3774-3783.
- S5. Zhang, L.; Wang, H., Cuprous Oxide Nanoshells with Geometrically Tunable Optical Properties. *ACS Nano* **2011**, *5*, 3257-3267.
- S6. Zhang, H.; Zhang, D.; Guo, L.; Zhang, R.; Yin, P.; Wang, R., One-Pot Assembly of Cu_2O Chain-Like Hollow Structures. *J. Nanosci. Nanotechnol.* **2008**, *8*, 6332-6337.